Materials Today Electronics 6 (2023) 100061

Contents lists available at ScienceDirect

Materials Today Electronics

journal homepage: www.elsevier.com/locate/mtelec

Valence band electronic structure of the van der Waals antiferromagnet $FePS_3$

Jonah Elias Nitschke [a,1], Dorye L. Esteras [b,1], Michael Gutnikov [a], Karl Schiller [a], Samuel Mañas-Valero [b], Eugenio Coronado [b], Matija Stupar [a], Giovanni Zamborlini [a], Stefano Ponzoni [a], José J. Baldoví [b,*], Mirko Cinchetti [a,*]

[a] TU Dortmund University, Otto-Hahn-Straße 4, Dortmund 44227, Germany
[b] Instituto de Ciencia Molecular (ICMol), Universidad de Valencia, c/Catedrático José Beltrán. 2, Paterna 46980, Spain

ARTICLE INFO

Keywords:
Transition-metal phosphotrichalcogenides
2D materials
angle-resolved photoemission spectroscopy
layered magnetism
antiferromagnetism

ABSTRACT

Antiferromagnetic van der Waals materials have gained a lot of interest in recent years. They can be exfoliated down to the two-dimensional (2D) limit while potentially preserving intriguing properties of antiferromagnets, such as insensitivity to external magnetic fields and ultrafast spin dynamics in the THz range. The investigation of the electronic band structure of these materials is crucial to understand their behavior and thus to identify paths for future applications. Here, we investigate the valence band structure of one of the most studied 2D antiferromagnets –iron phosphorus trisulfide ($FePS_3$)– using angle-resolved photoemission spectroscopy (ARPES) and compare our results with first-principles calculations based on Hubbard-corrected density functional theory (DFT+*U*). This allows us to identify the bands originating respectively from the Fe *3d*, the S *3p*, and the P *3p* orbitals and to describe their dispersion throughout the whole Brillouin zone. Our results represent an important step towards an accurate theoretical description of the electronic properties of transition metal phosphorus trisulfides, which is a pre-requisite for understanding the behavior of antiferromagnetic materials at the 2D limit.

Introduction

The exploration of 2D materials such as graphene and transition metal dichalcogenides (TMDs) has already led to numerous applications in modern technologies. With the discovery of magnetic van der Waals (vdW) layered materials that can be exfoliated even to single layers, also the investigation of 2D magnetic materials has attracted a growing interest in the past few years [1–4]. The possibility to study the fundamental behavior of magnetism at the 2D limit [2,4] and the ability to realize tuneable magnetic nanodevices with controlled strain, chemistry, optical and electrical properties [2,3,5] can open new paths for conceiving future spintronics [6–8] and magnonics devices [9–11].

Since the first detection of magnetic ordering in CrI_3 monolayer [12, 13], several 2D ferromagnets have been discovered and investigated, such as $MnSe_2$ [14], Fe_3GeTe_2 [15], VSe_2 [16] and $Cr_2Ge_2Te_6$ [4]. Even different spintronic devices could already be realized using some of the above-mentioned materials [17]. In the past years, also the research in antiferromagnetic materials experienced a sharp increase motivated by their insensitivity to external magnetic fields and their ultrafast spin dynamics in the terahertz frequency range [18,19] which could be beneficial for a variety of spintronic applications [20].

One of the most promising groups of 2D layered materials for the detailed study of antiferromagnetism down to the monolayer regime are the transition metal phosphorus trisulfides (MPS_3) [18,21–27] . In this family of intrinsic antiferromagnetic materials, the magnetic structure is defined by the honeycomb lattice built by the transition metal ions (M = Fe, Ni, Co, Mn) (see dark orange atoms in Fig. 1a and b). In a MPS_3 crystal, these metal ions are encapsulated by six S atoms (yellow) which are themselves connected by a P atom (magenta) above and below the Fe ions. Interestingly, these systems offer the possibility to study different kinds of models that describe magnetic ordering in two dimensions. In particular, $FePS_3$, $NiPS_3$, and $MnPS_3$ are considered as model systems for the Ising, XY- and Heisenberg model, respectively [21,28–31] (see Fig. 1c). Moreover, it was already proven in multiple cases that these materials are well suited for applications in future devices [32] due to their low separation energy as well as their stability in atmosphere [30].

* Corresponding authors.
E-mail addresses: j.jaime.baldovi@uv.es (J.J. Baldoví), mirko.cinchetti@tu-dortmund.de (M. Cinchetti).
[1] These authors contributed equally to this work.

https://doi.org/10.1016/j.mtelec.2023.100061
Received 25 April 2023; Received in revised form 30 August 2023; Accepted 4 September 2023
Available online 11 September 2023

For example, it has already been shown that $FePS_3$ can be successfully used to enhance the photoluminescence intensity of a MoS_2 monolayer [33].

Although the MPS_3 antiferromagnets have recently attracted quite a lot of attention, combined theoretical and experimental studies of their electronic band structure are still rare [34]. Here, we fill this gap by presenting micro-angle-resolved photoemission spectroscopy (μ-ARPES) data recorded on bulk $FePS_3$ crystals and comparing them with first-principles calculations based on Hubbard-corrected density functional theory (DFT+U). Our measurements unveil the rich band structure within the surface Brillouin zone (Fig. 1d), showing three main energy ranges dominated by multiple overlapping bands. Comparison with theory allows us to obtain a phenomenological U consistent with previous works. Furthermore, the calculated orbital-resolved electronic structure confirms the previous assignment of the main features in (angle-integrated) ultraviolet photoelectron spectroscopy (UPS) measurements reported by Piacentini et al. [26] and Miyazaki et al. [27]

Methods and experimental details

The $FePS_3$ crystals were commercially bought from HQ Graphene. They are glued with a UHV compatible glue containing silver particles on a copper dummy plate to ensure electrical contact with the ground and prevent charging of the sample during the measurements. After transfer in the UHV system, the crystals were exfoliated in a background pressure better than $3{\cdot}10^{-8}$ mbar with scotch tape to ensure a clean surface. The samples were then investigated by μ-ARPES with a KREIOS 150 MM momentum microscope by SPECS GmbH operating at a background pressure $< 3{\cdot}10^{-10}$ mbar [35]. This device allows to record 2D momentum maps, where the photoemission intensity is measured as a function of the parallel momenta (k_x,k_y) at a selected kinetic energy. The approximate momentum field-of-view is k_x, $k_y \in [-2.0 + 2.0]$ $\AA^{-1}$. The instrument is coupled to a p-polarized fs-XUV light source which uses the output of a pulsed 50 W CARBIDE fiber laser by Light Conversion with light pulses of 262 fs at 1030 nm and a repetition rate of 540 kHz. By focusing the second harmonic at 515 nm into an Ar gas jet, we utilize high-harmonic generation (HHG) to obtain XUV pulses with a photon energy of 21.7 eV (9th harmonic). After generation, the high-harmonic spectrum is filtered by successive grazing incidence plates, a 200 nm thick Al foil, and a monochromator based on multilayer coated mirrors. Focusing on the sample at 68° with respect to the normal surface with a spot size of a few hundred microns enables the excitation of photoelectrons from a locally flat surface, and thus to perform μ-ARPES experiments. The data shown in the following were acquired at a temperature of $T = 200$ K, which is above the Néel Temperature of $FePS_3$ ($T_N = 128$ K). Therefore, the shown spectra reflect the paramagnetic state of the $FePS_3$. The cooling was achieved by using liquid nitrogen throughout all the measurements. We would like to underline that we could not measure μ-ARPES spectra below T_N because crossing the critical temperature resulted in massive charging of the sample hindering the measurements.

Computational details

We performed DFT+U calculations using the QuantumESPRESSO software package [36]. The generalized gradient approximation (GGA) and the Perdew–Burke–Ernzerhof (PBE) [37] functional were used to describe the exchange-correlation energy. We selected standard solid-state ultra-soft (US) pseudopotentials. The electronic wave functions were expanded with well-converged kinetic energy cut-offs for the wave functions (75 Ry) and charge density (800 Ry). For the $FePS_3$ bulk structure, a non-magnetic configuration was considered in a primitive cell to correctly represent the crystal symmetry [31]. The highly localized d electrons of the Fe atoms were described by using an effective Hubbard U of 1.9 eV. The Brillouin zone was sampled by a fine Γ-centered 6 × 6 × 6 k-point Monkhorst–Pack [38] mesh in all calculations. Dispersion corrections to account for interlayer van der Waals interactions were considered by applying semi-empirical Grimme-D3 corrections [39,40]. We determined maximally-localized Wannier functions using a reduced basis set formed by the d orbitals of Fe, s and p orbitals of P and S atoms in the Wannier90 software [41]. We used the WannierTools package [42] to simulate theoretical momentum maps and ARPES. DFT surface state calculations were also carried out to benchmark the ARPES of WannierTools, were a 1 × 1 × 8 supercell was simulated to resolve layer by layer the contribution to the electronic band structure. Orbital resolved analysis was performed in a rotated system where the basis vectors were chosen to orient the axes along the ligands in the octahedral environment as indicated in Fig. S2.

Results and discussion

Fig. 2a shows the momentum map of the $FePS_3$ bulk crystal recorded at $\overline{E} = 5.15$ eV, where the energy scale is referenced to the valence band maximum (VBM) $\overline{E} = E^{kin}_{VBM} - E^{kin}$. The value of E^{kin}_{VBM} was extracted from the angle-integrated spectra as the kinetic energy where the intensity vanishes. The presented momentum map features different high-intensity spots aligned in a hexagonal pattern. These spots are located at the $\overline{M}$ points of the first surface projected Brillouin zone (BZ) as well as the $\overline{M}$ points of the neighboring BZ. This reflects the general symmetry of the first BZ of the crystal which is drawn in the image (white dotted lines) together with the high symmetry points $\overline{\Gamma}$, $\overline{K}$ and $\overline{M}$ of the surface BZ (see Fig. 1d for comparison). The hexagonal pattern can also be observed in various momentum maps recorded at other binding energies. Additionally, one can observe extra spots at higher $k_{||}$ which correspond to the $\overline{\Gamma}$ points of the neighboring BZ. This difference between the first and the neighboring BZ is either related to the k_z-dispersion of the electronic states close to the $\overline{\Gamma}$ point, similarly to the case of $ReSe_2$ [43] and ReS_2 [44], or to photoemission matrix element effects.

Based on the identified BZ, we extract from our dataset the band structure across different high symmetry points, which is presented in Fig. 2b and c. This is achieved by cutting the recorded data cube I(k_x, k_y,

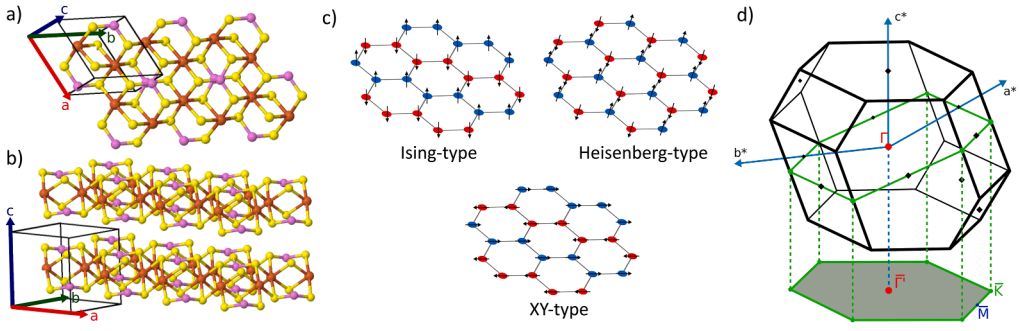

Fig. 1. (a) Top view on $FePS_3$ orthogonal to the lattice vectors a and b. The dark orange atoms show the hexagonal structure of the Fe atoms (the purple and yellow color correspond to the phosphor and sulfur atoms, respectively). (b) Side view of the $FePS_3$ with two layers. (c) Different types of 2D antiferromagnetic order. All three types are represented by the class of MPS_3 with $FePS_3$ (Ising), $NiPS_3$ (XY) and $MnPS_3$ (Heisenberg). (d) 3D Brillouin zone (BZ) of $FePS_3$ illustrating the surface projected BZ accessible by the photoemission study presented in this work.

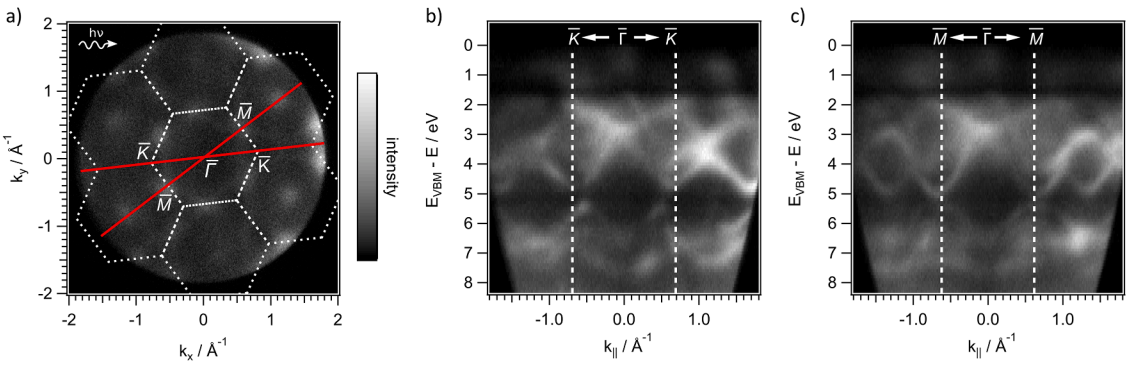

Fig. 2. Angle-resolved photoemission measurements acquired from $FePS_3$ with p-polarized light and a photon energy of 21.7 eV. (a) Momentum map for $FePS_3$ at 5.15 eV below the VBM. The white hexagons indicate the first surface BZ as well as the neighboring BZs. $\overline{\Gamma}$, $\overline{K}$ and $\overline{M}$ indicate the high symmetry points of the surface BZ. The direction of the incidence light beam lies parallel to the k_x-direction, impinging at 68° with respect to the surface normal. (b) Experimentally obtained band structure along the $\overline{K}-\overline{\Gamma}-\overline{K}$ direction. (c) Experimentally obtained band structure along the $\overline{M}-\overline{\Gamma}-\overline{M}$ direction.

$\overline{E}$) along the planes indicated by the red lines in Fig. 2a. In both the selected directions, the band structure shows three energy ranges with overlapping bands that are divided by two small gaps at 1.6–1.8 eV and 4.8–5.2 eV below the VBM, in agreement with previous angle-integrated photoemission measurements by Piacentini et al. [26] and Miyazaki et al. [27]. Our angle-resolved measurements unveil a rich band structure consisting of a mixture of rather localized bands (flat band dispersion), especially close to the VBM, and strongly dispersive bands for the 2nd and 3rd region between 1.8 and 8 eV below the VBM.

To reproduce and rationalize the experimental findings, we carried out first principles DFT+*U* calculations followed by a real space model based on maximally localized Wannier functions (see Computational details). The orbital-resolved electronic band structure is reported in Fig. 3, where we show the relative contributions of the *d* orbitals of Fe and *p* orbitals of S and P. In the absence of spin polarization, the *3d* orbitals of Fe split in fully occupied t_{2g} and empty e_g energy levels (Fig. S1), resulting in a low spin configuration that leads to 6 bands (3 per Fe atom in the unit cell) immediately below the Fermi level. By contrast, the *p* orbitals of P are mainly contributing at 5 eV. Finally, the bands located in the range 2–5 eV below the Fermi level, are mostly originated by the *p* orbitals of S, where the p_x orbital gives rise to the genuine dispersive pattern around the $\overline{\Gamma}$ point, whereas the p_z and p_y orbitals represent the edge between this pattern and the gap. The crystal and time reversal symmetry described by both primitive cell and spin unpolarized calculations, successfully describes the electronic structure of $FePS_3$ paramagnetic phase in agreement with the experiment. The octahedral coordination environment and the reference frame used to label the orbitals in terms of the computed Wannier functions are represented in Fig. S2.

We additionally performed the surface state analysis of $FePS_3$, where theoretical momentum maps and ARPES simulations were calculated using the software WannierTools. We compared the selected experimental and the corresponding theoretical momentum maps in the first BZ (see Fig. 4). The theoretical momentum maps confirm the surface states present the hexagonal patterns reported in the measurements and reveal their origin in the symmetry of the BZ. In fact, the complex BZ of the monoclinic structure is reduced to a perfect hexagon when $k_z = 0$, where the high symmetry points are situated in the corners ($\overline{K}$), center ($\overline{\Gamma}$) and the middle point of the sides ($\overline{M}$) in the hexagonal 2D reciprocal space. While most of the experimental momentum maps show the theoretically predicted hexagonal symmetry, some also display a trigonal symmetry. For example, one can easily identify a difference between $\overline{K}$ and $\overline{K}'$ for 5.75 eV below the VBM in Fig. 4a. This difference between theory and experiment is probably related to the k_z-dispersion of the electronic states probed in the photoemission experiments.

Fig. 5 shows the comparison of the ARPES measurement with the calculations along the $\overline{K}-\overline{\Gamma}-\overline{K}$ and $\overline{M}-\overline{\Gamma}-\overline{M}$ directions. We applied a curvature algorithm [45] to the ARPES data to increase the visibility of single bands, allowing a better comparison with the calculations. We observe an overall good agreement between experiment and theory, both along the $\overline{K}-\overline{\Gamma}-\overline{K}$ and the $\overline{M}-\overline{\Gamma}-\overline{M}$ directions. We would like to underline that in order to reproduce the experimental data, we applied a phenomenological Hubbard U of 1.9 eV, which allows to match the energy gap between the first and second group of bands. This value is in line with the previously reported values of U in this material (~2 eV) and compatible with the values used in previous publications from some of us to describe the electronic band gap [46] and electric [33] properties of this material. Guided by the experimental results we can thus confirm that such values result in a correct description of the electronic properties of $FePS_3$. To further check the effect of the choice of U on the theoretical results, we scanned the value of U between 0 and

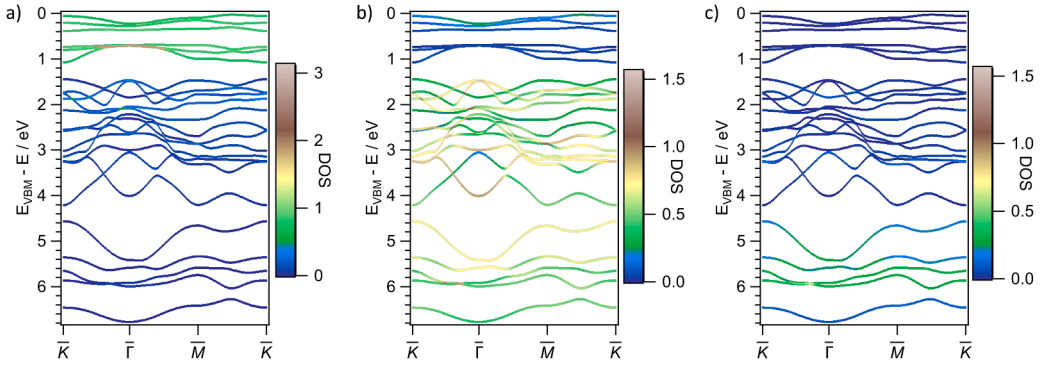

Fig. 3. Relative contributions to the DOS projected on the (a) Fe d-orbitals and the (b) and (c) p-orbitals of the elements S and P.

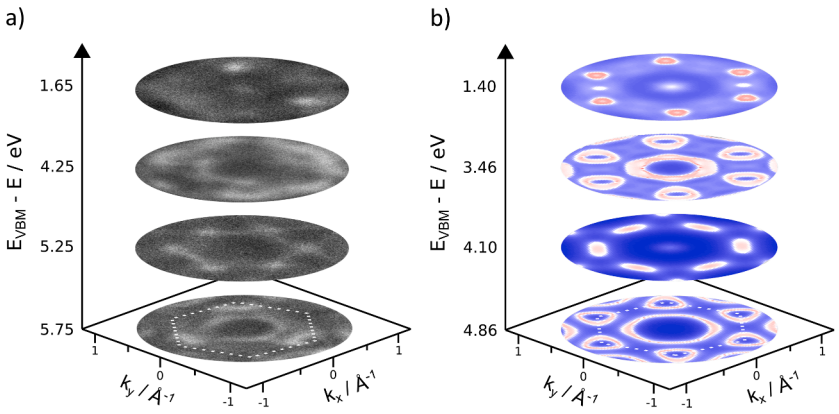

Fig. 4. (a) Experimental and (b) theoretical momentum maps for various energies. The first BZ is indicated in (a) with a white dotted line. The experimental data are plotted on a gray scale where black indicates zero photoemission intensity, while white indicates maximal intensity. Color scale in the theoretical data: red indicates pure surface states, white indicates pure bulk states and blue absence of bands.

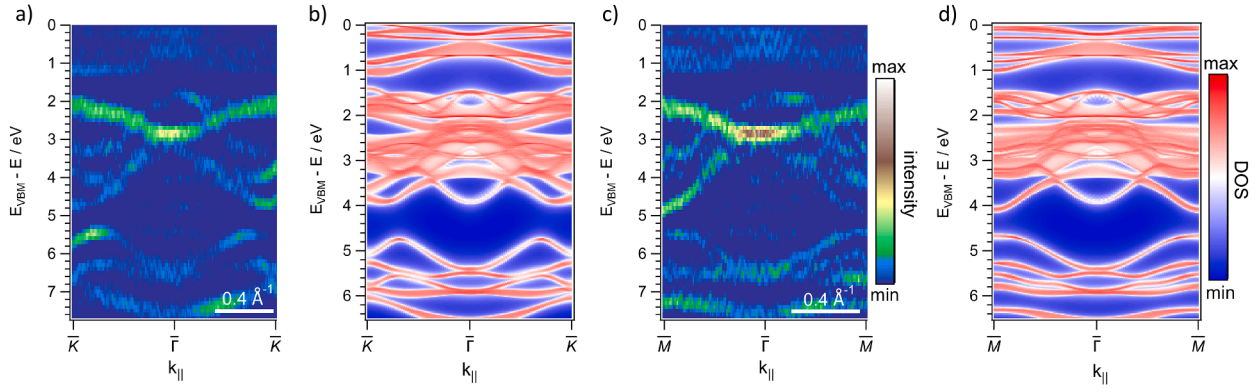

Fig. 5. Band structure of $FePS_3$ across the different high symmetry paths for (a,b) $\overline{K}-\overline{\Gamma}-\overline{K}$ and (c,d) $\overline{M}-\overline{\Gamma}-\overline{M}$ after applying the curvature algorithm [45] and the corresponding theoretical calculations obtained from Wannier Tools. Color scale in the theoretical data (b,d): red indicates pure surface states, white indicates pure bulk states and blue absence of bands.

4 eV. We found that its choice barely affects the dispersion of the bands but is crucial to describe the electronic gap found in the ARPES data (Fig. S3).

At this point, it is important to note that the surface electronic states obtained with WannierTools show many strongly overlapping bands. This limits a detailed comparison of single bands. However, the overall shape reproduces the experiment well. This can be especially observed at the high symmetry points of the BZ surface, as well as in the dispersion of the bands. The most prominent difference is the dispersion of the bands around 4–6 eV below the VBM. While the cut along the $\overline{M}-\overline{\Gamma}-\overline{M}$ direction shows maxima and minima of the bands at the high symmetry point, in the $\overline{K}-\overline{\Gamma}-\overline{K}$ direction the extrema are positioned slightly before the high symmetry points. To benchmark the WannierTools simulations, we perform a deep analysis of the surface states using a slab model formed by eight layers by means of DFT+*U*. Then, we resolve the electronic structure using an extended Wannier basis set that contains the same type of orbitals, namely, the *d* orbitals of Fe and the *s, p* orbitals of S and P. This allows us to obtain the electronic structure showing the individual contributions of each layer around $\overline{\Gamma}$ (Fig. S4). We can observe how the bands are arranged in packages formed by the contribution of the different layers, where the surface states are enveloped by the most internal ones. This evidences the relevance of interlayer van der Waals interactions in the electronic structure of MPS_3, allowing the selective tuning of the band structure by means of intercalation of ions or molecules in this class of 2D magnetic materials.

Conclusion

In summary, we provide the angle-resolved photoemission spectroscopy analysis of $FePS_3$ as a representative of the interesting and promising class of transition metal phosphorus trisulfides antiferromagnetic 2D materials. Our results unveil a rich band structure consisting of three main energy regions with multiple overlapping bands that are in excellent agreement with DFT+*U* first-principles calculations. The orbital resolved band structure reveals that the bands closer to the VBM are dominated by the Fe *3d* orbitals while the other two regions are mainly containing contributions from the *3p* orbitals of S and P. Comparison between theory and experiment allows us to determine an accurate value of U that leads to the best agreement with experiments. Our analysis paves the way to the precise description of the electronic properties of MPS_3, which is a necessary step for understanding and improving the performance of antiferromagnetic materials at the 2D limit.

Note: during the revision process of this manuscript, we became aware of a manuscript dealing with the same topic, see Ref. [47].

Declaration of Competing Interest

The authors declare that they have no known competing financial interests or personal relationships that could have appeared to influence the work reported in this paper.

Data availability

The raw data that support the findings of this study are available in the ZENODO database.

Acknowledgments

This work was supported by the Deutsche Forschungsgemeinschaft through the International Collaborative Research centre 160 (Projects B9 and Z4) and the TRR 142/3, Project A08. We acknowledge support from the European Union's Horizon 2020 Research and Innovation Programme under Project SINFONIA, Grant 964396 and ERC-StG-101042680 2D-SMARTiES. We also thank the Spanish MICINN (2D-HETEROS PID2020–117152RB-100, co-financed by FEDER, and Excellence Unit "María de Maeztu" CEX2019–000919-M), and the Plan Gent of Excellence of the Generalitat Valenciana (Grants No. CDEIGENT/2019/022 and CIDEGENT/2018/004). The Momentum Microscope has been financed by the Deutsche Forschungsgemeinschaft (DFG) through the project INST 212/409 and by the "Ministerium für Kultur und Wissenschaft des Landes Nordrhein-Westfalen". The computations were performed on the Tirant III cluster of the Servei d'Informàtica of the University of Valencia.

Supplementary materials

Supplementary material associated with this article can be found, in the online version, at doi:10.1016/j.mtelec.2023.100061.

References

[1] M. Gibertini, M. Koperski, A.F. Morpurgo, K.S. Novoselov, Magnetic 2D materials and heterostructures, Nat. Nanotechnol. 14 (2019) 408–419.
[2] K.S. Burch, D. Mandrus, J.G. Park, Magnetism in two-dimensional van der Waals materials, Nature 563 (2018) 47–52.
[3] J.G. Park, Opportunities and challenges of 2D magnetic van der Waals materials: magnetic graphene? J. Phys. Condens. Matter 28 (2016), 301001.
[4] C. Gong, et al., Discovery of intrinsic ferromagnetism in two-dimensional van der Waals crystals, Nature 546 (2017) 265–269.
[5] S. Rahman, J.F. Torres, A.R. Khan, Y. Lu, Recent developments in van der Waals antiferromagnetic 2D materials: synthesis, characterization, and device implementation, ACS Nano 15 (2021) 17175–17213.
[6] E.C. Ahn, 2D materials for spintronic devices, npj 2D Mater. Appl. 4 (2020) 17.
[7] J.F. Sierra, J. Fabian, R.K. Kawakami, S. Roche, S.O. Valenzuela, Van der Waals heterostructures for spintronics and opto-spintronics, Nat. Nanotechnol. 16 (2021) 856–868.
[8] X. Lin, W. Yang, K.L. Wang, W. Zhao, Two-dimensional spintronics for low-power electronics, Nat. Electron. 2 (2019) 274–283.
[9] T.T. Mai, et al., Magnon-phonon hybridization in 2D antiferromagnet MnPSe3, Sci. Adv. 7 (2021) 3106–3135.
[10] D.L. Esteras, A. Rybakov, A.M. Ruiz, J.J. Baldoví, Magnon straintronics in the 2D van der Waals ferromagnet CrSBr from first-principles, Nano Lett. 22 (2022) 8771–8778.
[11] W. Xing, et al., Magnon transport in quasi-two-dimensional van der Waals antiferromagnets, Phys. Rev. X 9 (2019), 011026.
[12] B. Huang, et al., Layer-dependent ferromagnetism in a van der Waals crystal down to the monolayer limit, Nature 546 (2017) 270–273.
[13] B. Huang, et al., Electrical control of 2D magnetism in bilayer CrI3, Nat. Nanotechnol. 13 (2018) 544–548.
[14] D.J. O'Hara, et al., Room temperature intrinsic ferromagnetism in epitaxial manganese selenide films in the monolayer limit, Nano Lett. 18 (2018) 3125–3131.
[15] Y. Deng, et al., Gate-tunable room-temperature ferromagnetism in two-dimensional Fe_3GeTe_2, Nature 563 (2018) 94–99.
[16] M. Bonilla, et al., Strong room-temperature ferromagnetism in VSe_2 monolayers on van der Waals substrates, Nat. Nanotechnol. 13 (2018) 289–293.
[17] Z. Wang, et al., Tunneling spin valves based on Fe_3GeTe_2/hBN/Fe_3GeTe_2 van der Waals heterostructures, Nano Lett. 18 (2018) 4303–4308.
[18] F. Mertens, et al., Ultrafast coherent THz lattice dynamics coupled to spins in the van der Waals antiferromagnet $FePS_3$, Adv. Mater. 35 (2022), 2208355.
[19] O. Gomonay, V. Baltz, A. Brataas, Y. Tserkovnyak, Antiferromagnetic spin textures and dynamics, Nat. Phys. 14 (2018) 213–216.
[20] T. Jungwirth, X. Marti, P. Wadley, J. Wunderlich, Antiferromagnetic spintronics, Nat. Nanotechnol. 11 (2016) 231–241.
[21] J.U. Lee, et al., Ising-type magnetic ordering in atomically thin $FePS_3$, Nano Lett. 16 (2016) 7433–7438.
[22] K. Kim, et al., Suppression of magnetic ordering in XXZ-type antiferromagnetic monolayer $NiPS_3$, Nat. Commun. 10 (2019) 345.
[23] K. Kim, et al., Antiferromagnetic ordering in van der Waals 2D magnetic material MnPS3 probed by Raman spectroscopy, 2D Mater. 6 (2019), 041001.
[24] S. Kang, et al., Coherent many-body exciton in van der Waals antiferromagnet $NiPS_3$, Nature 583 (2020) 785–789.
[25] M. Piacentini, V. Grasso, S. Santangelo, S. Modesti, Soft X-ray absorption of $FePS_3$ and $NiPS_3$, Solid State Commun. 51 (1984) 467–471.
[26] M. Piacentini, et al., Study of the valence bands of $FePS_3$ and NiPS by resonant-photoemission spectroscopy, Nuovo Cimento D 4 (1984) 444–452.
[27] T. Miyazaki, et al., UPS study of $NiPS_3$ and $FePS_3$ crystals using synchrotron radiation, Chem. Phys. 201 (1995) 539–546.
[28] D. Lançon, et al., Magnetic structure and magnon dynamics of the quasi-two-dimensional antiferromagnet $FePS_3$, Phys. Rev. B 94 (2016).
[29] X. Wang, et al., Raman spectroscopy of atomically thin two-dimensional magnetic iron phosphorus trisulfide ($FePS_3$) crystals, 2D Mater. 3 (2016).
[30] K.Z. Du, et al., Weak Van der Waals stacking, wide-range band gap, and Raman study on ultrathin layers of metal phosphorus trichalcogenides, ACS Nano 10 (2016) 1738–1743.
[31] C.T. Kuo, et al., Exfoliation and Raman spectroscopic fingerprint of few-layer $NiPS_3$ Van der Waals crystals, Sci. Rep. 6 (2016) 20904.
[32] R. Kumar, R.N. Jenjeti, M.P. Austeria, S. Sampath, Bulk and few-layer $MnPS_3$: a new candidate for field effect transistors and UV photodetectors, J. Mater. Chem. C Mater. 7 (2019) 324–329.
[33] M. Ramos, et al., Photoluminescence enhancement by band alignment engineering in MoS_2/$FePS_3$ van der Waals heterostructures, ACS Appl. Mater. Interfaces 14 (2022) 33482–33490.
[34] J. Strasdas, et al., Electronic band splittings across the antiferromagnetic phase transition of exfoliated MnPS3 probed by μ-ARPES. 10.48550/arXiv.2211.05501.
[35] S. Ponzoni, et al., Dirac bands in the topological insulator Bi_2Se_3 mapped by time-resolved momentum microscopy, Adv. Phys. Res. 2 (5) (2023), 2200016.
[36] P. Giannozzi, et al., Quantum espresso: a modular and open-source software project for quantum simulations of materials, J. Phys. Condens. Matter 21 (2009), 395502.
[37] J.P. Perdew, K. Burke, M. Ernzerhof, Generalized gradient approximation made simple, Phys. Rev. Lett. 77 (1996) 3865–3868.
[38] H.J. Monkhorst, J.D. Pack, Special points for Brillonin-zone integrations, Phys. Rev. B 13 (1976) 5188–5192.
[39] S. Grimme, Semiempirical GGA-type density functional constructed with a long-range dispersion correction, J. Comput. Chem. 27 (2006) 1787–1799.
[40] W. Setyawan, S. Curtarolo, High-throughput electronic band structure calculations: challenges and tools, Comput. Mater. Sci. 49 (2010) 299–312.
[41] A.A. Mostofi, et al., Wannier90: a tool for obtaining maximally-localised Wannier functions, Comput. Phys. Commun. 178 (2008) 685–699.
[42] Q. Wu, S. Zhang, H.F. Song, M. Troyer, A.A. Soluyanov, WannierTools: an open-source software package for novel topological materials, Comput. Phys. Commun. 224 (2018) 405–416.
[43] L.S. Hart, et al., Electronic bandstructure and van der Waals coupling of $ReSe_2$ revealed by high-resolution angle-resolved photoemission spectroscopy, Sci. Rep. 7 (2017) 5145.
[44] M. Gehlmann, et al., Direct observation of the band gap transition in atomically thin ReS_2, Nano Lett. 17 (2017) 5187–5192.
[45] P. Zhang, et al., A precise method for visualizing dispersive features in image plots, Rev. Sci. Instrum. 82 (2011), 043712.
[46] M. Ramos, et al., Ultra-broad spectral photo-response in FePS3 air-stable devices, npj 2D Mater. Appl. 5 (2021) 19.
[47] A. Koitzsch, et al., Intertwined electronic and magnetic structure of the van-der-Waals antiferromagnet Fe2P2S6, npj Quantum Mater. 8 (2023) 27.